Structure and Optical Properties of Some Middle-Level Clouds

C. M. R. PLATT

Division of Atmospheric Physics, CSIRO, Aspendale, Victoria, Australia

K. BARTUSEK[1]

Dept. of Physics, University of Adelaide, Adelaide, South Australia

(Manuscript received 11 June 1973, in revised form 28 December 1973)

ABSTRACT

Simultaneous infrared (10–12 μm) and visible (0.694 μm) optical properties of some altocumulus and altostratus clouds have been determined using infrared radiometry and lidar.

Broadly, two types of middle-level clouds were observed; rather thin (~200 m) dense clouds forming between 0 and −5C and with high infrared absorption coefficients (~8 km^{-1}), and thicker, low-density clouds, forming between −10 and −30C and with average infrared absorption coefficients of less than 1 km^{-1}. The former type were undoubtedly liquid water clouds, whereas the latter were probably ice or mixed-phase clouds. Both types were often semi-transparent to infrared radiation.

Lidar backscatter coefficients for the higher clouds were typically between 0.1 and 3 km^{-1}.

The experimental backscatter-to-extinction ratio at 0.694 μm and the ratio of the backscatter at 0.694 μm to the absorption at 10–12 μm are compared with theoretical computations. In certain cases, changes in these ratios could be identified with changes in the cloud microstructure.

Calculated infrared cooling rates in the clouds varied from 0.1 to 1.5C hr^{-1} depending on cloud density.

1. Introduction

Simultaneous measurements of the optical properties of cirrus clouds with an infrared radiometer (10 to 12 μm) and a laser radar (lidar) at 0.694 μm wavelength have been described in Platt (1973) [hereafter referred to as I], and Platt and Gambling (1971). These measurements formed part of a larger program aimed at investigating the infrared and visible optical properties of real cloud systems; this article reports some similar measurements made on middle-level altocumulus and altostratus clouds.

The two quantities measured in I were the infrared (IR) cloud radiance in the 10 to 12 μm wavelength interval and the lidar (visible) cloud backscatter amplitude at different heights in the clouds at 0.694 μm wavelength. As the cloud altitude was given by the lidar, the theoretical blackbody infrared cloud radiance at the cloud center could be computed from aerological data, and the cloud emissivity was obtained from the ratio of the measured cloud radiance to the blackbody radiance. Also, the cloud backscatter coefficients were obtained by calibrating the lidar against known Rayleigh backscatter coefficients from clear air.

It was shown in I that correlation of the infrared emissivity and the experimental, visible-integrated backscatter (the visible backscatter coefficient integrated through the cloud depth) led to a value for the cloud visible backscatter-to-extinction ratio. This ratio was utilized to correct the experimental visible cloud backscatter coefficients for attenuation of the laser pulse by the cloud. Although cloud multiple scattering effects caused the experimental backscatter-to-extinction ratio (but not the corrected backscatter coefficients) to deviate from its true value, this deviation could be inferred in cases where sufficient good experimental data were available.

In this article, IR emissivities and visible backscatter coefficients of some altocumulus clouds are presented and compared with cirrus clouds, using the same techniques as in I. Additionally, the ratios of various measured visible and IR quantities are compared with values obtained from Mie theory computations on model cloud droplet distributions as well as experimental ratios obtained for cirrus clouds. Theoretically, appreciable differences in the above ratios between various droplet distributions should be apparent, and these would be different again for cirrus ice clouds.

Finally, some preliminary computations on the IR cooling in some model altocumulus clouds are presented, based on the cloud properties reported in this article.

The only optical measurements on altocumulus clouds reported recently were the infrared emissivity (8–13 μm) measurements of Allen (1971) and the multispectral solar transmission measurements reported by

[1] Present affiliation: Weapons Research Establishment, Box 2151, G.P.O. Adelaide, South Australia.

Grassl (1970). Allen used stereophotography to infer cloud base altitude and hence the blackbody radiance, but the cloud thickness and internal structure could not be determined. Grassl was able to specify a cloud droplet distribution fairly closely by the use of 10 spectral intervals used simultaneously between 0.477 and 27.4 μm and his measured quantities agreed well with theory. The main virtues of the present techniques are that measurements can be made at any time of day or night and at any elevation (although the lidar was fixed in the zenith in the present measurements), and that the lidar gives information on the cloud's internal structure and it spatial and temporal variations. No lidar measurements on altocumulus clouds have, to the author's knowledge, been previously reported.

The cloud optical quantities and ratios used in the comparison of experiment and theory are discussed in the next section.

2. Cloud IR and visible optical quantities

a. *Cloud extinction coefficients, backscatter coefficients and optical thicknesses*

The volume extinction coefficient σ of a cloud at a given wavelength can be written

$$\sigma=\sum_j \pi Q_j n_j a^2, \tag{1}$$

where the extinction efficiency Q_j and the number density n_j are summed over all droplet radii a_j. The backscatter coefficient $B(\pi)$ (over 4π steradians) is similarly defined by replacing Q_j in (1) by the backscatter efficiency $\beta(\pi)$. At 0.694 μm wavelength the absorption efficiency is negligible and extinction is due to scattering. The visible scattering efficiency is defined as Q_v. At 10–12 μm the absorption efficiency Q_{abs} and scattering efficiency Q_{sca} are comparable (see I). However, the effects of scattering are reduced considerably as the scattering is forward-peaked (see Section 4a). Thus, Q_{abs} can be used to describe the IR emission properties of the cloud.

The cloud optical thickness τ is defined as $\tau=\sigma h$ for a homogeneous cloud of depth h. The integrated backscatter coefficient $\gamma(\pi)$ is defined as $\gamma(\pi)=B(\pi)h$. For an inhomogeneous cloud, τ and $\gamma(\pi)$ are given by the corresponding integral equations. The visible and IR (absorption) optical thicknesses are defined as τ_v and τ_A, respectively. All symbols are made consistent with I.

b. *Relations between visible and IR quantities*

Experimental quantities which can be calculated from the measurements and which are characteristic of the cloud as a whole, are the visible and IR optical thicknesses and the integrated lidar backscatter. The backscatter-to-extinction ratio k can be found from combined IR and visible data. The quantities k, $\gamma(\pi)/\tau_A$ and α will be used to compare experiment and theory and are defined as

$$k=B(\pi)/\sigma_v, \tag{2}$$

$$\gamma(\pi)/\tau_A=B(\pi)h/(\sigma_A h)=B(\pi)/\sigma_A, \tag{3}$$

$$\alpha=\tau_v/\tau_A=\sigma_v h/\sigma_A h=\sigma_v/\sigma_A, \tag{4}$$

where σ_v and σ_A are the visible extinction coefficient and the IR absorption coefficient, respectively. The above equations imply that the cloud is homogeneous in density and has a droplet size distribution which is constant with height in the cloud. (However, it can be shown that the equations are equally valid if the cloud droplet number density varies with height, as long as the *distribution* remains the same). Although the size distribution is not constant with height in most real clouds, the assumptions are sufficient to distinguish gross changes in cloud microstructure.

For comparison with experiment two cloud droplet distributions have been chosen. Distribution 1, considered by Deirmendjian (1964), has the analytical formula $n(a)=2.373a^6e^{-1.5a}$, with a mode radius $a_c=4$ μm. Distribution 2 was taken from Grassl (1970) for a lenticular altocumulus. Similar clouds were observed at Adelaide. Distribution 2 has a mode radius of 2.2 μm, being otherwise similar to distribution 1. Mie computations of Q_v and $\beta(\pi)$ were taken from Brinkworth (1971) and Mie values of Q_{abs} from Irvine and Pollack (1968). Values of k, $\gamma(\pi)/\tau_A$ and α using the above figures in equations similar to Eq. (1) are shown in Table 1. The mean experimental values found for cirrus in I are also shown. The values of $\gamma(\pi)/\tau_A$ for the two droplet distributions are seen to differ markedly, but k is rather constant. The behavior of k and $\beta(\pi)/Q_{\text{abs}}$ [i.e., $\gamma(\pi)/\tau_A$] with increasing radius for *monodisperse* clouds are shown in Fig. 1. Where k is not sensitive to radius a, $\beta(\pi)/Q_{\text{abs}}$ decreases with increasing a. The parameter $\alpha[=Q_v/Q_{\text{abs}}]$ has a value of 8.5 at 2 μm radius, decreasing to 2 at 10 μm radius, thereafter remaining constant. These properties account for the variations in Table 1. The low cirrus values have been discussed in I. The backscatter coefficient is much lower for ice crystals due, it is thought, to their non-spherical shape (see, for instance, Liou, 1972).

3. Experimental method

Full details of the lidar and infrared radiometer are given in I. The infrared radiometer had a narrow beam-

TABLE 1. Theoretical cloud optical quantities.

Cloud model	$\gamma(\pi)/\tau_A$	k	α
Distribution 1	1.86	0.64	3.19
Distribution 2	3.30	0.67	4.91
Cirrus	0.47*	0.26*	1.84**

* Experimental values from I.
** Theoretical value assuming an ice particle cross section equal to that of a 50-μm sphere.

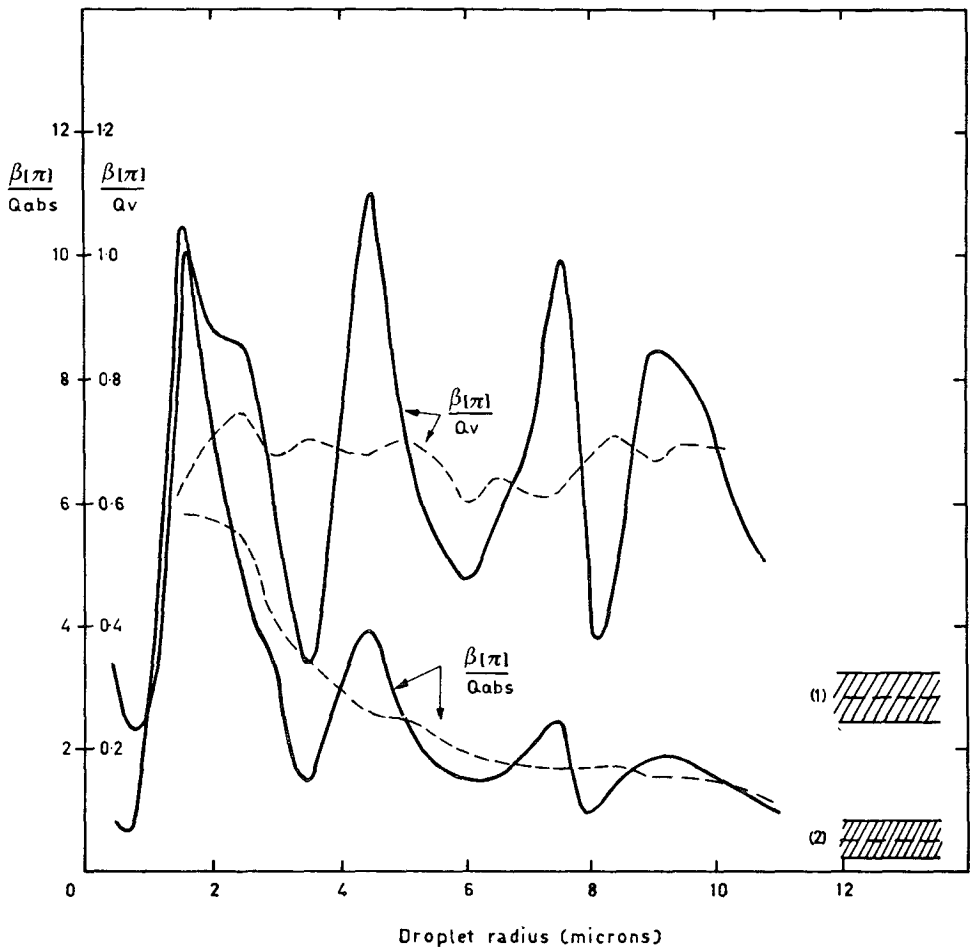

FIG. 1. Theoretical values of $\beta(\pi)/Q_v$ and $\beta(\pi)/Q_{abs}$ as a function of water droplet radius a for a visible wavelength of 0.694 μm and an infrared wavelength of 11 μm; full lines, values averaged over 0.2-μm intervals; broken lines, values averaged over 2.5-μm intervals. Cross-hatching (1) indicates experimental range of values of $\beta(\pi)/Q_v$ for cirrus clouds (Platt, 1973) and $\eta=0.4$; (2) indicates experimental range of values of $\gamma(\pi)/\tau_A$ [i.e., $\beta(\pi)/Q_{abs}$] for cirrus clouds (Platt, 1973).

width of 6 mrad and contained a filter which isolated the 10–12 μm spectral region. The lidar transmitter and receiver beamwidths were 1 and 5 mrad, respectively, the pulse length was 0.5 μsec, and the wavelength 0.694 μm. The radiometer measured the cloud infrared radiance continuously as a departure from the background "clear-sky" value. The lidar backscatter profile was displayed on an oscilloscope and photographed, and this limited the firing rate to a maximum of one per minute. The lidar and radiometer were set up to view in the zenith and operated as described in I.

4. Experimental analysis

a. Determination of cloud infrared emissivity and infrared optical thickness

The cloud infrared emissivity ϵ was calculated as the ratio of the measured cloud radiance to the theoretical blackbody radiance at mid-cloud temperature. The error in ϵ through using a *mid*-cloud temperature has been investigated. For a cloud 1 km thick, $\epsilon=0.25$ is 1% too low and $\epsilon=0.9$ is 4% too low. Corrections to the radiance were made for water vapor absorption between the cloud and the ground (see I). Two scattering effects also had to be considered. First, upwelling warm earth radiance was reflected downward by the clouds, thereby increasing the measured downward radiance by up to 10%. This was computed and subtracted from the measured radiance (see I). Second, scattering of *emitted* radiation within the cloud also increased the downward radiance. However, this increase was only 1% in cirrus clouds (I) and about 4% in liquid water clouds (Zdunkowski and Choronenko 1969) and this magnitude of error was small within the overall data accuracy. This being so, the absorption optical thickness τ_A of the cloud could be related to its emissivity ϵ by the formula (Hall, 1968)

$$\tau_A=\ln(1-\epsilon). \quad (5)$$

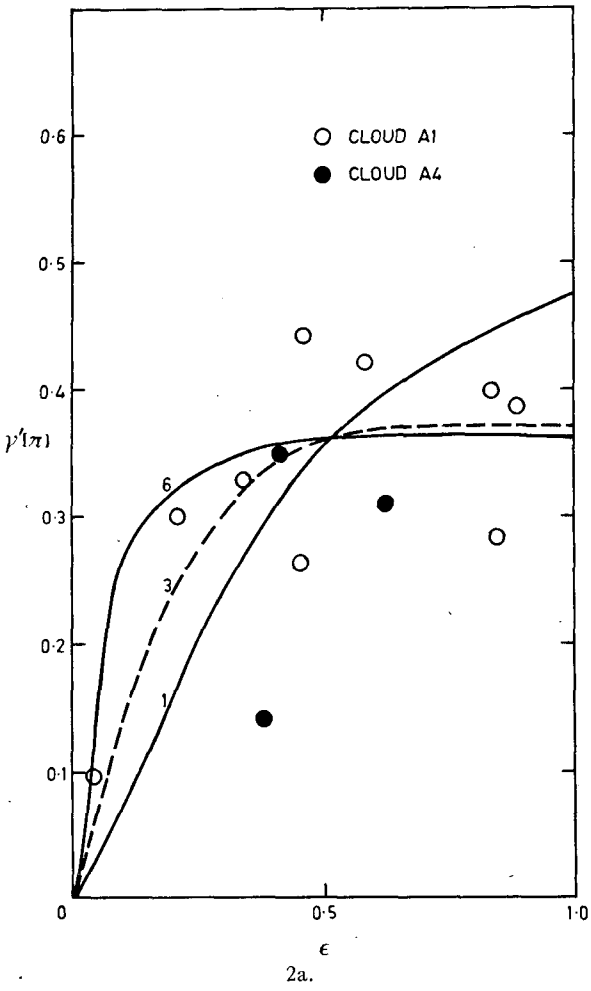

2a.

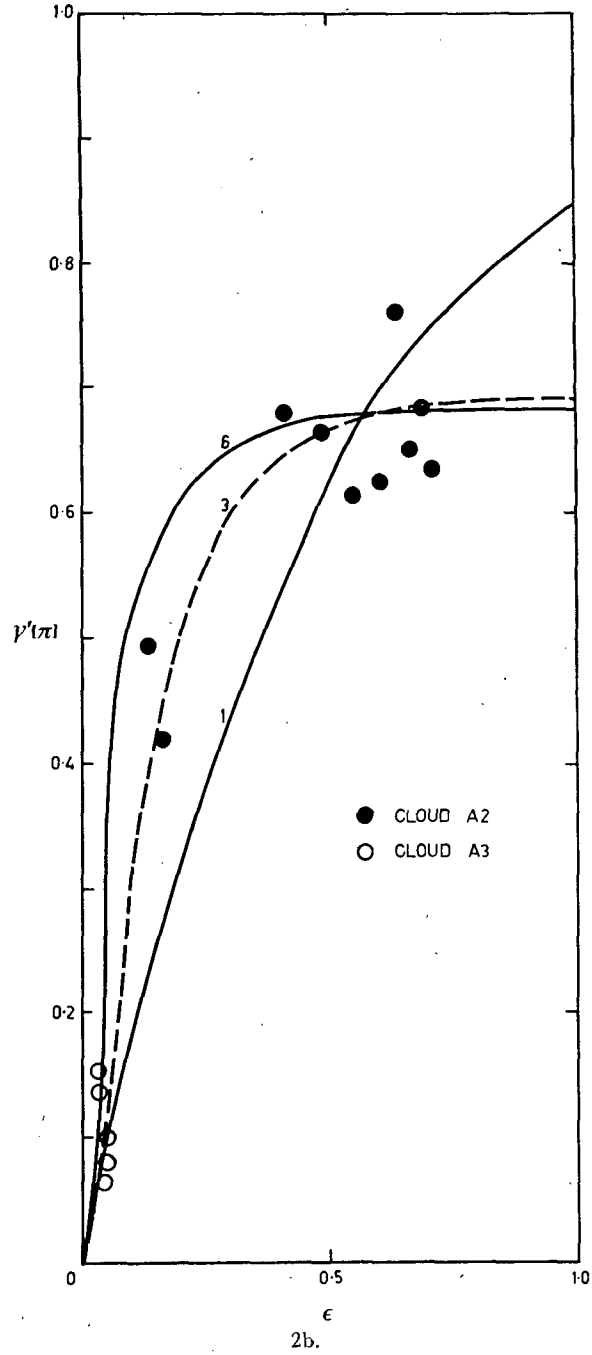

2b.

FIG. 2. Integrated lidar backscatter $\gamma'(\pi)$ vs infrared emissivity ϵ for altocumulus clouds A1, A4 (Fig. 2a) and A2, A3 (Fig. 2b). Theoretical curves are calculated from Eq. (A5) for values of the parameter $\alpha\eta = 1, 3, 6$.

A mean cloud infrared absorption coefficient $\bar{\sigma}_A[=\tau_A/h]$ was calculated at the time of each lidar sounding.

b. Determination of experimental lidar cloud backscatter coefficients and backscatter-to-extinction ratios

The object of the lidar analysis was to obtain values of the backscatter coefficient $[B(\pi,z)]$, integrated backscatter through the cloud $[\gamma(\pi)=\int B(\pi,z)dz]$, and the backscatter-to-extinction ratio k. Lidar backscatter amplitudes were read from the polaroid photographs at height intervals of 37.5 m and corrected for range and background clear air backscatter. They were then converted to backscatter coefficients by comparison with backscatter amplitudes when there was no cloud in the zenith, and at a height where the aerosol contribution was estimated to be small (see I). The theoretical Rayleigh molecular backscatter was computed from the aerological data.

Because of the attenuation of the laser pulse within the cloud, the experimental cloud backscatter coefficient, as calculated above [denoted by $B'(\pi,z)$] is less than the true backscatter coefficient $B(\pi,z)$. In fact, as shown in Appendix A,

$$B'(\pi,z)=B(\pi,z)\exp[-2\eta\tau_v(z)], \qquad \text{(A2)}$$

where the apparent cloud optical thickness $\eta\tau_v(z)$ is measured from the cloud base z_0 to altitude z. $\tau_v(z)$ is given in terms of $\sigma_v(z)$ and depth h, and η accounts for multiple scattering in the laser beam (Appendix B).

TABLE 2. Experimental cloud optical quantities.

Cloud no.	Cloud type	Date	Height of base (km)	Cloud depth (km)	Temperature range (°C)	ϵ	τ_A	$\bar{\sigma}_A$ (km^{-1})	$\gamma(\pi)$	$\gamma(\pi)/\tau_A$	$k/2\eta$	k^*
A1	altocumulus	11/23/70	5.6	1.1	−15 to −19	0.58	1.1	0.96	0.83	1.13±0.2	0.4 ±0.04	0.66 ± 0.20
A2	altocumulus	11/23/70	4.6	1.6	−10 to −17	0.53	0.8	0.64	1.49	2.08±0.4	0.7 ±0.07	1.23 ± 0.37
A3	altocumulus	11/23/70	4.5	1.5	−10 to −17	0.03	0.03	0.02	0.11	>3	—	—
A4	altocumulus	23/11/70	4.6	1.0	−10 to −14	0.56	1.1	0.84	0.46	0.64±0.1	0.4 ±0.04	0.66 ± 0.20
A5	altocumulus	24/11/70	4.0	0.25	−4 to −5	0.80	—	8	—	—	—	—
A6	altocumulus	5/ 8/72	2.9	0.6	−1 to −4	0.25	0.29	0.4	0.12	0.38±0.08	0.27 ±0.05	0.40 ± 0.15
A7	altostratus	5/ 8/72	5.1	1.8	−13 to −30	0.92	2.37	1.1	0.99	0.42±0.08	0.37 to 0.51	0.55 to 0.76±0.1
A8**	altocumulus	11/24/71	3.9	0.2	−5	0.5	—	11	—	—	—	—

* $\eta = 0.75$.
** Aircraft observation (see text).

Mean cirrus values obtained in reference I.
$\gamma(\pi)/\tau_A = 0.47 \pm 0.1$
$k/2\eta = 0.33 \pm 0.04$
$k = 0.26 \pm 0.06$
$\eta = 0.42 \pm 0.14$

In order to correct the backscatter coefficients for cloud attenuation an *experimental* backscatter-to-extinction ratio k/η for each cloud was required [k/η relates $B(\pi,z)$ to the apparent cloud extinction coefficient $\eta\sigma_v(z)$]. A method of obtaining k/η is given below.

The experimental integrated backscatter

$$\gamma'(\pi) = \int_{z_0}^{z_0+h} B'(\pi,z)dz$$

was first computed for each lidar sounding by numerical integration of the experimental backscatter coefficients. It is shown in Appendix A that $\gamma'(\pi)$ is related to the corresponding infrared emissivity ϵ by

$$\gamma'(\pi) = (k/2\eta)\left\{1-\exp\left[-2\eta\alpha \ln\left(\frac{1}{1-\epsilon}\right)\right]\right\}, \quad \text{(A5)}$$

where it is assumed that α and η both remain constant through the cloud depth and that η is independent of optical thickness. (The validity of the second assumption is discussed in Appendix B.)

Eq. (A5) shows that $\gamma'(\pi) = k/2\eta$ when $\epsilon = 1$. Plots of $\gamma'(\pi)$ vs ϵ are shown in Figs. 2a and 2b for values of $\alpha\eta$ equal to 1, 3 and 6. For typical droplet distributions $\alpha\eta \approx 2$–4. If $\alpha\eta > 3$ then Figs. 2 show that $\gamma'(\pi) \approx k/2\eta$ if $\epsilon \gtrsim 0.5$. In that case a plot of values of $\gamma'(\pi)$ vs corresponding values of ϵ yields a value for $k/2\eta$, as long as ϵ becomes greater than 0.5.

If many corresponding values of $\gamma'(\pi)$ and ϵ are available, then a plot of these data will yield an estimate also of the quantity $\alpha\eta$. In I, such plots were possible between $\gamma'(\pi)$ and the infrared optical thickness τ_A [instead of ϵ; see Eq. (A4)], and the scatter in the results was low enough to specify both $k/2\eta$ and $\alpha\eta$. In the present results there was never a sufficient range of values of $\gamma'(\pi)$ and ϵ in any one cloud to be able to specify a value of $\alpha\eta$ with any confidence. However, Figs. 2a and 2b indicate that as long as $\alpha\eta \gtrsim 1$, $k/2\eta$ could be determined with an accuracy commensurate with the experimental data.

c. Determination of true backscatter coefficient

Values of $B(\pi,z)$ were obtained by inversion of Eq. (A2) and computation of the experimental optical depth $\eta\tau_v(z)$ cumulatively through the cloud in height steps of 37 m, starting at the base. The method involved an iterative procedure whereby values of $B'(\pi,z)$ were used initially to compute "first-try" values of $\eta\sigma_v(z)$ and $\eta\tau_v(z)$ for each step using the estimated value of k/η (see I).

5. Estimates of error

The errors in the determination of ϵ were estimated to be ±50% at $\epsilon = 0.05$ reducing linearly to ±8% at $\epsilon = 0.7$. The backscatter coefficient $B'(\pi)$ was subject to both random and systematic error. The random error was caused mainly by fluctuations in the laser pulse power (~±10%). The systematic error was due to the assumption of negligible aerosol backscatter at calibration height (~10 km). This assumption was estimated to cause a maximum error in $B'(\pi)$ from about ±20% to 30%. Percentage errors in $\gamma'(\pi)$ were carried over unchanged from $B'(\pi)$. However, changing conditions within the cloud with time obviously increased the "random" scatter in $\gamma'(\pi)$ (e.g., Fig. 2a), thus increasing the error in the determination of k/η. The error in k/η was also due to the uncertainty in the value of $\alpha\eta$.

The errors in the corrected parameters $B(\pi)$ and $\gamma(\pi)$ depended on both the errors in $\gamma'(\pi)$ and the corresponding value of ϵ. This is because errors in $k/2\eta$ have a greater effect on $\gamma(\pi)$ when ϵ is large than when ϵ is small. If, due to a random error in $\gamma'(\pi)$ at a high value of ϵ, $\gamma'(\pi)$ becomes *greater* than $k/2\eta$, then the computation of $B(\pi,z)$ and $\gamma(\pi)$ becomes unstable. In this case $k/2\eta$ had to be artificially raised until stability was restored.

The error in $k/2\eta$ caused errors in the *relative* values of $B(\pi)$ in a single cloud profile, and values near the cloud *top* were affected more than those near the cloud base. However, the positions of the maxima in $B(\pi)$ were affected only slightly.

6. Results and discussion

Average values of cloud emissivity ϵ, cloud height, and cloud depth for each cloud are shown in Table 2, along with calculated values of τ_A and $\bar{\sigma}_A$ (see

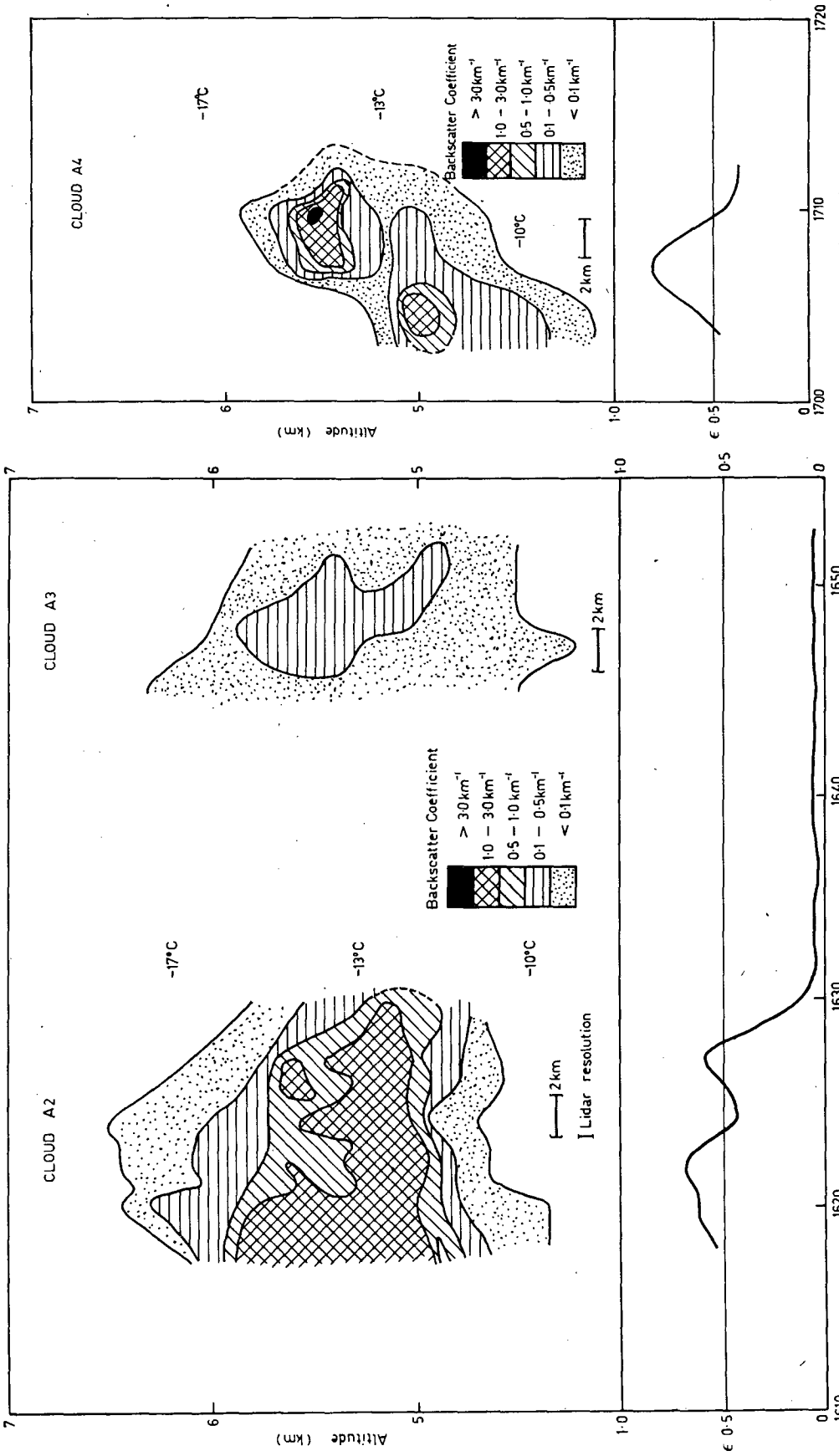

FIGS. 3a and 3b. Time-height profiles of visible backscatter coefficients in the zenith, and infrared emissivities ϵ. Clouds A2 and A3.

FIG. 3c. As in Figs. 3a,b. Cloud A4.

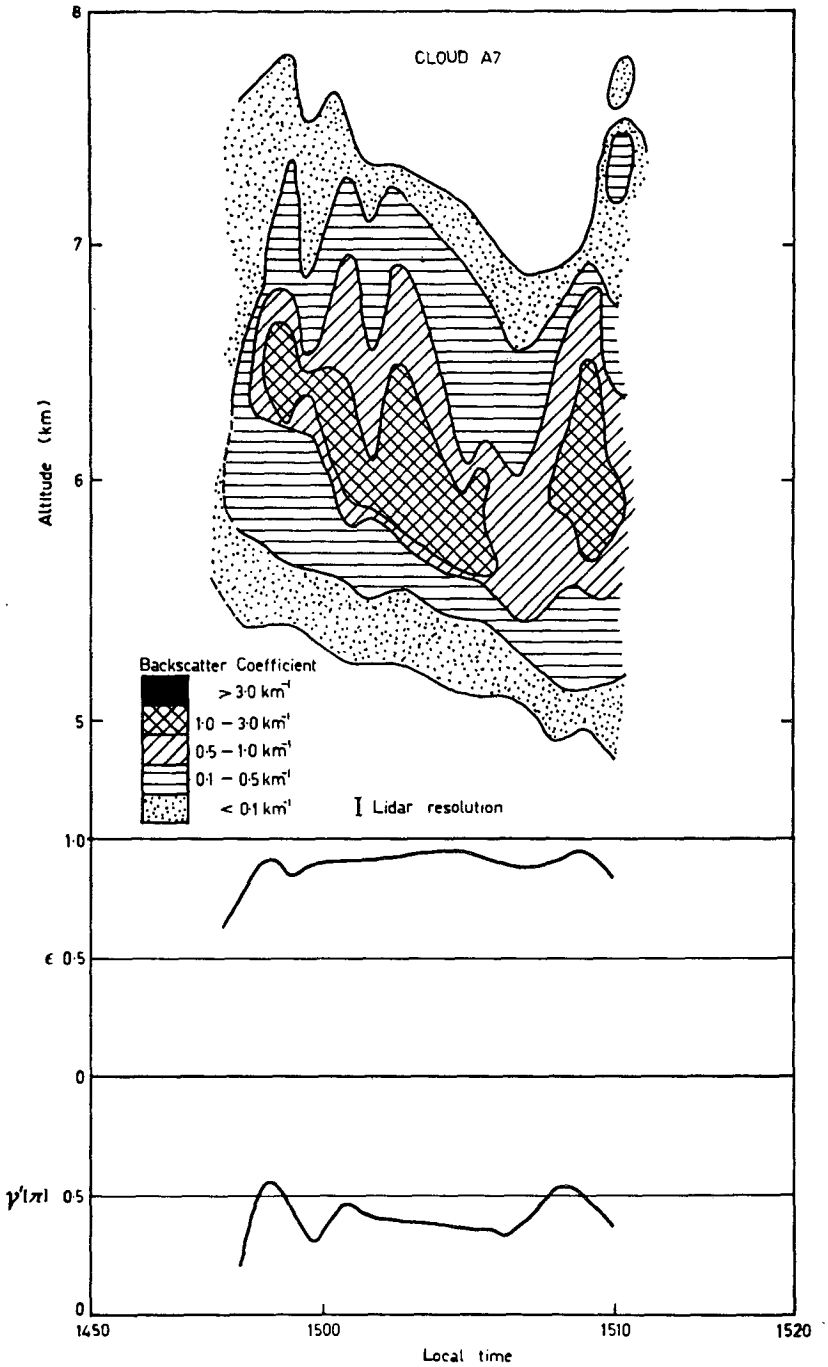

FIG. 3d. As in Fig. 3a. Cloud A7. Plot of $\gamma'(\pi)$ also included.

Section 4a). The number of lidar observations on each cloud varied from 4 to 20. The other columns in Table 2 show calculated mean values of $\gamma(\pi)$, $\gamma(\pi)/\tau_A$, $k/2\eta$ and k for each cloud. The latter values were calculated assuming $\eta=0.75$, which is considered to be a mean value for all cloud types (Appendix B). The indicated errors in the above quantities have been evaluated in Section 5.

Examples of cloud backscatter coefficients from zenith lidar firings at minute intervals are shown plotted as contours in a time-height representation in Figs. 3a–3d. The figures are thus *evolutionary* pictures of the clouds as they drifted through the zenith. The horizontal dimensions of the clouds were estimated from Adelaide wind data at cloud height. Values of IR emissivity ϵ are also shown.

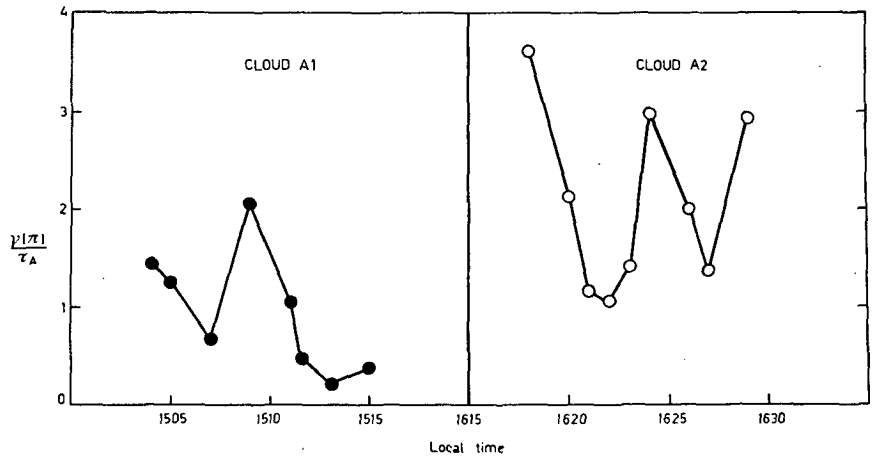

FIG. 4. Time variation of the experimental ratio $\gamma(\pi)/\tau_A$ for two altocumulus clouds.

The above results illustrate the wide variations in optical properties to be found in middle-level clouds. Clouds A5 and A8 have absorption coefficients ($\sim$10 km^{-1}) which are typical of water droplet clouds, such as stratocumulus. [A8 was measured on a separate aircraft flight; the techniques have been described in Platt (1972).] The clouds observed within the range of -10 to -30C had mean infrared absorption coefficients <1 km^{-1}, although the cloud depths were frequently 1–2 km. These clouds were most likely composed of both supercooled water droplets and ice crystals and their properties are discussed further below in terms of the quantities $\gamma(\pi)/\tau_A$ and k.

The evolutionary cloud contour plots of backscatter coefficients show much internal cloud structure. If the cloud particle phases and size distributions were constant, then the backscatter coefficients would be proportional to cloud liquid water content. Variations in droplet size distributions could cause an estimated 30% change in values of $B(\pi,z)$ for a given cloud water content. Changes in phase from water to ice could decrease $B(\pi,z)$ by a factor of $2\frac{1}{2}$ for a given water content. In practice, values of $B(\pi,z)$ changed frequently by a factor of 10 or more, so that the variations in backscatter coefficients do give a guide to changes in cloud liquid water content. The typical situation for stratocumulus and convective clouds where the liquid water content is a maximum near the cloud tops (Borovikov *et al.*, 1963) is exhibited by cloud A4 (Fig. 3c). In clouds A2 and A7 the maximum occurs near the cloud center, as found in some frontal clouds investigated (Borovikov *et al.*) as well as in cirrus clouds (Reference I and Heymsfield and Knollenberg, 1972).

The average experimental values of $\gamma(\pi)/\tau_A$ and k (Table 2) lie within the ranges either predicted for droplet clouds or measured for cirrus clouds (Table 1). Taking individual cases, clouds A2 and A3 gave high values of $\gamma(\pi)/\tau_A$ and k, consistent with either water cloud distribution 1 or 2. However, the measured value of k for cloud A2 was higher than that predicted for either droplet distribution. Cloud A3 had a very low IR emissivity of 0.03. Visually, this "cloud" was a milky-blue patch of sky *outside* the "visible" edge of cloud A2, after A2 had drifted away from the field of view. It probably represented a precondensation or evaporation phase with a population of very small supercooled droplets. The values of $\gamma(\pi)/\tau_A$ and k for the other clouds examined lay between the water droplet and cirrus ice crystal values, indicating possibly the existence of both water drops and ice crystals in the cloud in varying proportions.

Variations of $\gamma(\pi)/\tau_A$ with time within two individual clouds are shown in Fig. 4. These variations are greater than the estimated experimental error and possibly represent changes in droplet distribution or phase with time. It is estimated that pointing errors between the radiometer and lidar could have caused about 30% of this variation at the most.

Cloud A7, which was identified as altostratus, had a heavy grey appearance and an emissivity ϵ which remained close to unity. This being so, variations in $\gamma'(\pi)$ with time would indicate changes in $k/2\eta$. Such variations did indeed occur in a systematic manner. A plot of $\gamma'(\pi)$ is shown in Fig. 2d. At two times, $\gamma'(\pi)$ (and hence $k/2\eta$) approached 0.6, possibly indicating the formation of supercooled droplets within these regions. It is interesting that the region of maximum backscatter in this cloud is "falling" at a rate of 50 m min^{-1} which is similar to the observed rate of fall of typical hexagonal ice crystals (Heymsfield, 1972). It is possible that the regions of high $k/2\eta$ represented volumes of newly condensed supercooled droplets which were subsequently growing into ice crystals and falling through the cloud (Heymsfield and Knollenberg, 1972).

7. Infrared cooling rates in altocumulus clouds

Three cloud models with properties similar to those described above have been used to give an estimate of

TABLE 3. Mean rate of cooling (°C hr^{-1}) in given cloud layers for three cloud models.

Cloud model	Layer extent (km)	Total depth (km)	Transmission*	ϵ**	σ†	Cooling rate	Clear sky cooling rate
M1	4.2 –5.1		0.75		0.32	−0.08	0.07
M1	5.1 –5.9		0.55		0.75	0.18	0.07
M1	5.9 –6.6	2.4	0.75	0.70	0.32	0.38	0.07
M2	4.2 –5.1		0.92		0.10	0.035	0.07
M2	5.1 –5.9		0.75		0.32	0.175	0.07
M2	5.9 –6.6	2.4	0.92	0.37	0.10	0.15	0.07
M3	3.45–3.70	0.25	0.01	0.95	12	1.5	0.07

* Zenith transmission through each layer.
** Total emissivity of cloud.
† Cloud absorption coefficient (km^{-1}).

infrared cooling rates in altocumulus clouds. A Rodgers-Walshaw type scheme (G. W. Paltridge, private communication) was used to compute mean cooling rates within the layers. Typical mid-latitude temperature and humidity profiles were used for all the computations. Realistic variations in these quantities would only alter the cooling rate detail, but not its order of magnitude. Cooling rates (°C hr^{-1}) are shown in column 7 of Table 3, along with the layer extents, IR transmission of the layers, and the total cloud emissivity. Corresponding "clear air" cooling rates are shown in column 8. It was assumed that the cloud was a grey body, with no spectral changes in transmission, and scattering effects were neglected.

Clouds M1 and M2 represent typical deep cloud layers (e.g., A7 and A2). It can be observed that the cooling per hour is only a fraction of a degree. Lenticular altocumulus clouds such as A2 were not observed to exist for longer than 1 hr so that their formation and dissipation could not have been greatly affected by IR radiation. Cloud M3 represents a rather thin and dense layer of altocumulus, or stratocumulus. The mean cooling in a cloud 0.25 km deep is 1.5C hr^{-1}, which is likely to have an effect on the cloud dynamics (Paltridge, 1974), or even the cloud microstructure.

8. Conclusion

The experimental values of both $\gamma(\pi)/\tau_A$ and $k/2\eta$ in Table 2 lie within the ranges of the theoretical values for either the model cloud distributions or the experimental values for cirrus. This is an encouraging result and indicates that the method of calibration of the lidar amplitudes is reliable. Moreover, the altocumulus clouds are often sufficiently transparent to enable the laser pulses to pass through the total extent of the cloud yielding information on the internal cloud structure. Comparison of IR and lidar data gives some broad information on cloud microstructure.

Important assumptions made in the analysis are that η is independent of cloud optical thickness and of variations in cloud density, and that the ratios $\alpha[=\tau_v/\tau_A]$ and k are constant everywhere within a given cloud. Further theoretical and computational work is required to assess the importance of the above assumptions in the derivation of cloud optical quantities, particularly lidar backscatter quantities.

An independent determination of cloud phase would assist in the interpretation of the results. Recent work by Schotland *et al.* (1971) indicates that ice crystals depolarize the plane-polarized lidar transmitter beam in the back direction, whereas water droplets do so only slightly. Preliminary measurements made by the authors on cirrus clouds in May 1972 support Schotland's results. Although more work is needed, the method promises to be very useful.

Preliminary computations of infrared cooling indicate that the cooling is only 0.1–0.3C hr^{-1} throughout the cloud if the cloud has an absorption coefficient of about 0.5–1 km^{-1}, even for a 2 km deep cloud. However, dense layers of water cloud of absorption coefficients of about 5–10 km^{-1} exhibit intense cooling of 1.5C hr^{-1}, or greater. It is thus important to determine the frequencies with which each cloud occurs in order to gauge their effects on the radiation budget of the atmosphere and the effects of cooling on the clouds themselves.

APPENDIX A

A Relation between the Cloud Visible Integrated Backscatter $\gamma'(\pi)$ and the Cloud Infrared Emissivity ϵ

The measured backscatter at a height z is affected by the attenuation of molecules, aerosols and cloud particles between the ground and height z. However, the calibration clear-sky backscatter amplitude (Section 4b) is measured at a height which is greater than or comparable with the cloud height. Thus, the measured clear-sky amplitude has suffered nearly the same attenuation (to within 1%) as the measured cloud amplitude, and the experimental cloud backscatter coefficient $B(\pi,z)$ can be regarded as being affected only by cloud attenuation. Then $B'(\pi,z)$ is given by

$$B'(\pi,z)=B(\pi,z)\exp(-2\eta\tau_v), \qquad \text{(A1)}$$

where $B(\pi,z)$ is the true backscatter coefficient, τ_v the visible cloud optical thickness, and η a factor which accounts for multiple scattering (see Appendix B). Denoting the integral of $B'(\pi,z)$ through the cloud as $\gamma'(\pi)$, we have

$$\gamma'(\pi)=\int_{z_0}^{z_0+h} B(\pi,z)\exp[-2\eta\tau_v(z)]dz. \quad \text{(A2)}$$

Using the relations $B(\pi,z)=k\sigma_v(z)$ from Eq. (2) and $d\tau=\sigma_v(z)dz$, and integrating (A2) yields

$$\gamma'(\pi)=(k/2\eta)[1-\exp(-2\eta\tau_v)]. \quad \text{(A3)}$$

If the ratio τ_v/τ_A is denoted by α, and α is assumed to be independent of cloud depth, then (A3) can be written

$$\gamma'(\pi)=(k/2\eta)[1-\exp(-2\eta\alpha\tau_A)], \quad \text{(A4)}$$

or, from Eq. (5), as

$$\gamma'(\pi)=(k/2\eta)\left\{1-\exp\left[-2\eta\alpha\ln\left(\frac{1}{1-\epsilon}\right)\right]\right\}, \quad \text{(A5)}$$

which is the required relation.

APPENDIX B

Multiple Scattering and the Apparent Value of the Lidar Visible Optical Thickness

Multiple scattering in the laser beam causes more energy to be returned to the receiver than by single scattering alone. Thus, the apparent cloud optical thickness which is deduced from the analysis (Section 3c) is less than the optical thickness for single scattering. Multiple scattering is significant, even within the narrow lidar receiver beam because of the well-known peaking of the Mie phase function in the forward direction for particles with large size parameters. Generally, the value of η [see (A1)] will be smaller for a high cloud of large particles and larger for a low cloud of small particles. Kattawar and Plass (1971) calculated the ratios of multiple-to-single-scattered laser energy returned to the lidar receiver. Converting their ratios to values of η gave $\eta=0.84$ for a 1 km deep stratus cloud at 1 km altitude and $\eta=0.6$ for a 1 km deep cirrus cloud at 9 km altitude. Also, their results showed that for a *homogeneous* cloud, η was independent of visible optical thickness τ_v, at least for $\tau_v<5$.

The path taken by multiple scattered radiation reflected from a layer in a cloud and returned to the receiver, is typically 1 m longer than single scattered radiation from the same layer. This is only a small fraction of the lidar resolution of 75 km, so that the problem can be treated as time-independent.

REFERENCES

Allen, J. R., 1971; Measurements of cloud emissivity in the 8–13 μ waveband. *J. Appl. Meteor.*, **10**, 260–265.

Borovikov, A. M., A. Kh Khrgian, and others, 1963: *Cloud Physics*. Israel Program for Scientific translations, 392 pp.

Brinkworth, B. J., 1971: Calculations of attenuation and backscattering in cloud and fog. *Atmos. Environ.*, **5**, 605–611.

Deirmendjian, D., 1964: Scattering and polarization properties of water clouds and hazes in the visible and infrared. *Appl. Opt.*, **3**, 187–196.

Grassl, H., 1970: Determination of cloud drop size distribution from spectral transmission measurements. *Beitr. Phys. Atmos.*, **43**, 255–284.

Hall, F. F., Jr., 1968: A physical model of cirrus 8 μm to 13 μm sky radiance. *Appl. Opt.*, **7**, 2264–2269.

Heymsfield, A. J., 1972: Ice crystal terminal velocities. *J. Atmos. Sci.*, **29**, 1348–1357.

——, and R. G. Knollenberg, 1972: Properties of cirrus generating cells. *J. Atmos. Sci.*, **29**, 1358–1366.

Irvine, W. H., and J. B. Pollack, 1968: Infrared optical properties of water and ice spheres. *Icarus*, **8**, 324–360.

Kattawar, G. W., and G. N. Plass, 1971: Reflection of light pulses from clouds. *Appl. Opt.*, **10**, 2304–2310.

Liou, Kuo-Nan, 1972: Light scattering by ice clouds in the visible and infrared: A theoretical study. *J. Atmos. Sci.*, **29**, 524–536.

Paltridge, G. W., 1974: Atmospheric radiation and the gross character of stratiform cloud. *J. Atmos. Sci.*, **31**, 244–250.

Platt, C. M. R., 1972: Airborne infrared radiance measurements (10- to 12-micron) off tropical east-coast Australia. *J. Geophys. Res.*, **77**, 1597–1609.

——, 1973: Lidar and radiometer observations of cirrus clouds. *J. Atmos. Sci.*, **30**, 1191–1204.

——, and D. J. Gambling, 1971: Emissivity of high layer clouds by combined lidar and radiometric techniques. *Quart. J. Roy. Meteor. Soc.*, **97**, 322–325.

Schotland, R. M., K. Sassen and R. Stone, 1971: Observations by lidar of linear depolarization ratios for hydrometeors. *J. Appl. Meteor.*, **10**, 1011–1017.

Zdunkowski, W. G., and I. Choronenko, 1969: Incompleteness of clouds in the infrared spectrum. *Beitr. Phys. Atmos.*, **42**, 206–223.